IEEE Access
Multidisciplinary | Rapid Review | Open Access Journal

Received April 23, 2020, accepted May 5, 2020, date of publication May 11, 2020, date of current version May 26, 2020.

Digital Object Identifier 10.1109/ACCESS.2020.2993812

Three-Dimensional Ground-Based SAR Imaging Algorithm Based on Keystone Formatting and Subblock

WEIMING TIAN[1,2,3], WENYU YANG[1], TONGXIN DANG[4], ZHENG ZHAO[1], AND XIAOXIN HAN[1]

[1]Radar Research Laboratory, School of Information and Electronics, Beijing Institute of Technology, Beijing 100081, China
[2]Beijing Institute of Technology Chongqing Innovation Center, Chongqing 401120, China
[3]Key Laboratory of Electronic and Information Technology in Satellite Navigation, Beijing Institute of Technology, Ministry of Education, Beijing 100081, China
[4]PLA Strategic Support Force Information Engineering University, Zhengzhou 450002, China

Corresponding author: Tongxin Dang (samurano@qq.com)

This work was supported in part by the National Natural Science Foundation of China under Grant 61971037.

ABSTRACT Three-dimensional (3D) ground-based synthetic aperture radar (GB-SAR) draws attention because of the ability to obtain high accuracy 3D information of the monitoring terrain. Besides, the 3D GB-SAR system is welcome due to the flexibility and large coverage in angle and range. However, existing 3D imaging algorithms for GB-SAR data focusing have limits of high computational complexity or narrow applicable scope. To realize 3D displacement monitoring with high spatial resolution and short revisit time, in this paper, a novel 3D imaging algorithm is proposed. Based on characteristics of the model of echo data from the large range and wide-view angle scenario, the proposed method uses keystone formatting to complete range migration correction and subblocks dechirping to realize horizontal focus. With the method, the reflectivity of the monitoring scenario is obtained by only one time of linear interpolation and several times of fast Fourier transforms. The main advantages of this algorithm are high imaging precision and low computational cost, and in addition, it is applicable for large illuminating coverage including the near-field and the far-field of the radar aperture. The imaging results are sampled on pseudo-spherical grid, aiming to simplify the formulation. Finally, this method is extensively validated with simulations.

INDEX TERMS Synthetic aperture radar (SAR), ground-based SAR (GB-SAR), three-dimensional (3D) imaging algorithm, keystone formatting, subblocks.

I. INTRODUCTION

Ground-based synthetic aperture radar (GB-SAR), a newly rising synthetic aperture radar technology, can realize large-area, all-weather and all-time monitoring with high accuracy and short revisit time. In addition, the GB-SAR system applies the differential interference (DIn) techniques of space-borne SAR to catch up the deformation in millimeter or even sub-millimeter precision. Therefore, it is widely used for deformation monitoring of open pit mines [1], [2], landslides [3], [4], buildings and structures [5] and glacier snow mountains [6], [7].

The conventional two-dimensional (2D) GB-SAR imaging system can only acquire an image which actually is a two-dimensional projection on the range-azimuth plane of the natural three-dimensional space. Therefore, the 3D GB-SAR system is adopted to obtain targets' height information. It obtains two-dimensional large aperture through the radar motion in azimuth and height directions which enables it to have azimuth and height resolutions, and further realizes 3D high precision imaging combined with transmission of the large time-bandwidth signal. In practical application, DInSAR system is used to obtain the tiny deformation of the 3D monitored terrain. The key step of the processing is the registration of the radar image and 3D DEM (Digital Elevation Model) [8]. That is corresponding the pixel points of the radar image to the points in the 3D DEM. And the deformation information of the 3D DEM can be obtained by the deformation of the corresponding pixel points. However, the 2D radar image can only obtain the 2D information of

The associate editor coordinating the review of this manuscript and approving it for publication was Gerardo Di Martino.

the 3D monitored terrain, so only the 2D deformation information of 3D terrain can be gotten. On the contrast, after the registration of the 3D radar image and 3D DEM, every point of the 3D DEM can be match to the pixel points of the 3D radar image. Based on the 3D GB-DInSAR technique, the 3D deformation information of the pixel points can be obtained, so the 3D displacement information of 3D terrain can be gotten without the information loss. In addition, 3D GB-DInSAR system can be used to achieve the 3D deformation monitoring of snow mountains, landslides, volcanoes or manmade structures. The tomographic 3D GB-SAR system can be used to measure the high-dimensional information of snow mountains. For example, the SAPHIR team utilized a tomographic 3D GB-SAR system transmitting signals in X-band and Ku-band to obtain the vertical structure of snow mountains and such natural environment [9]. Stephen Joseph Preston and David G. Long made use of 3D GB-SAR to monitor snowpacks [10], [11].

The key issue of 3D GB-SAR system is the fast and accurate imaging algorithm. The echo data produce the 3D radar image after imaging processing, so the processing computational cost directly determines the system's real-time performance. The back projection algorithm (BPA) is a widely used algorithm because of its high precision and simplicity. In addition, it can be easily used in SAR systems with all kinds of configurations. However, BPA's high computational cost makes it not suitable for large-scale and fast-deforming monitoring. Even though there are some proposed methods to improve BPA's performance [12], [13], it still cannot meet the requirements of dealing with the fast-changing phenomenon. Reference [14] has proposed a far-field pseudopolar format algorithm (FPFA). It only retains one-term in the range history of targets. Therefore, FPFA is only valid in near-field even if it is fast to focus data. There is a wavenumber domain imaging algorithm, RMA [15] It obtains the spatial spectrum of targets from the echo data, then combined with deformation, filling and etc. of the spatial spectrum to obtain the scattering function of the whole scene. However, the stolt interpolation process of RMA is a necessary step but has high computational load [16], [17]. Thus, RMA is not applicable for real-time imaging of 3D GB-SAR.

This paper proposes an efficient and accurate 3D imaging algorithm, that is Three Dimensional Keystone formatting and Subblock Dechirping (3D-KSD) algorithm. The core of this algorithm is the range cell migration correction (RCMC) and horizontal dechirping processing [18], [19], where the RCMC is realized by keystone formatting, and the horizontal focusing can be achieved by subblocks dechirping operation. The approximate preserving quadratic terms of the range history makes 3D-KSD algorithm suitable for near-field and far-field focusing. At the same time, because of the only once keystone formatting and several fast Fourier transforms (FFT), it has a low computational cost. Besides, the number of horizontal subblocks decreases with the range increasing, which reduces the computational cost further. Thus, the algorithm can achieve fast focus of a wide and large scene.

This paper is organized as follows. In Section II, the principle of three-dimensional imaging radar is elaborated and the mathematical model of pulse-compressed echo signal is given, based on which the imaging algorithm is presented in detail. In addition, the application conditions and computational complexity of the algorithm are discussed. In Section III, the validation of the algorithm is extensively summarized with the simulated data and a comparison with BPA and FPFA is illustrated. Finally, our conclusions are outlined in Sections IV.

II. THE BASIS OF THE THREE-DIMENSIONAL GROUND-BASED SAR SYSTEM

The 3D GB-SAR system achieves cross-range resolutions in azimuth and height directions by a 2D synthetic aperture. Here, the fuzzy function is applied to analyze the resolution performance of the 3D GB-SAR system, whose data collection geometry is shown in FIGURE 1.

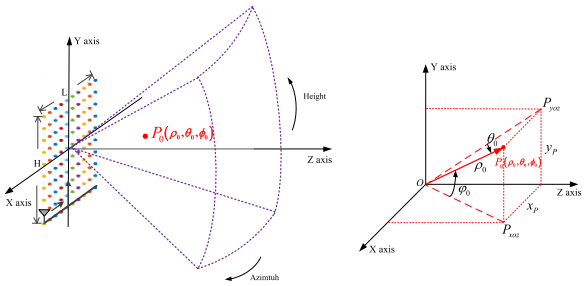

FIGURE 1. 3D GB-SAR system data collection geometry and the three dimensional pseudo-spherical coordinates of the point target.

The antenna moves in the track as the arrow along the x direction shows. When the antenna arrives at the end of the track, the track moves up the distance between two sample points as the arrow along the y direction shows. Thus, we can see that the length of the track is L which is the synthetic aperture in the azimuth direction, and the distance that the track moves is H which is the synthetic aperture in the height direction. The movement of antenna in $x-y$ plane achieves two-dimensional synthetic aperture. The colored dots on the $x-y$ plane are the sampled points of two-dimensional synthetic aperture where the antenna transmits and receives signal and correspondingly the antenna location is $P(n, i) = (x_n, y_i, 0)$. The three-dimensional area enclosed by the purple dotted line is the detection area of the 3D GB-SAR system. There is one point target $P_0(\rho_0, \theta_0, \phi_0)$ in the area. To avoid data redundancy, the imaging result is formed in a pseudo-spherical coordinate where the target's location is $P_0(\rho_0, \theta_0, \phi_0)$. Different with spherical coordinate, the azimuth angle θ_0 is the angle between the OP_0 vector and the y-z plane, and the height angle ϕ_0 is the one between the vector and the x-z plane. ρ_0 is the distance from P_0 to the aperture center O ($|OP_0|$) shown as the right picture in FIGURE 1.

Transmitting signal of the system is chirp signal, which is $s_t(t) = rect\left(\frac{t}{T_p}\right)\exp(j2\pi f_c t)\cdot\exp(j\pi Kt^2)$. t is the fast time; T_p is the pulse width; f_c is the carrier frequency; K is the chirp rate. And the range history from the target $P_0(\rho_0, \theta_0, \phi_0)$ to the antenna $P(n, i)$ is:

$$R(n, i; P_0) = \sqrt{x_n^2+y_i^2+\rho_0^2-2x_n\cdot\rho_0\sin\theta_0-2y_i\cdot\rho_0\sin\phi_0} \quad (1)$$

Thus, the echo signal from P_0 is:

$$\begin{aligned} &s_r(t, x_n, y_i; P_0) \\ &= s_t\left(t-2R(n, i; P_0)/c\right) \\ &= \text{rect}\left(\frac{t-\tau_{n,i}}{T_p}\right)\exp\left(j2\pi f_c\left(t-\tau_{n,i}\right)\right)\exp\left(-j\pi K(t-\tau_{n,i})^2\right) \end{aligned} \quad (2)$$

where $\tau_{n,i} = 2\cdot R(n, i; P_0)/c$ is the time delay of target P_0.

The fuzzy function was first proposed by J.Ville, and has become an effective mathematical tool for studying radar signal and getting its resolution performance. Here, we use the fuzzy function to analyze the range resolution, azimuth resolution and height resolution of 3D GB-SAR system. The fuzzy function is defined by the correlation operation between the echo signal and the transmitting signal [20], [21]. So it is written as, (3) shown at the bottom of the next page.

where the integral term is the range fuzzy function $\chi_R(\tau_{n,i})$. The range resolution is determined by

$$A_r = \frac{\int_{-\infty}^{\infty}|\chi_R(\tau)|^2\,d\tau}{\chi_R^2(0)} = \frac{\int_{-\infty}^{\infty}|U(f)|^4\,df}{\left|\int_{-\infty}^{\infty}|U(f)|^2\,df\right|^2} \quad (4)$$

where A_r is the delay resolution constant; $U(f)$ is amplitude spectrum of the transmitting signal. And (3) can be written as:

$$\chi(n, i; P_0) = \sum_{n=1}^{N}\sum_{i=1}^{I}\exp\left(j2\pi f_c\tau_{n,i}\right)\cdot\chi_R(\tau_{n,i}) \quad (5)$$

Since the point P_0 is in the far field of the system, the $\tau_{n,i}$ is as follows using Taylor expansion at P_0:

$$\tau_{n,i} = \frac{2R(n, i; P_0)}{c} = \frac{2\left(\rho_0-\sin\theta_0\cdot x_n-\sin\phi_0\cdot y_i\right)}{c} \quad (6)$$

Thus, (5) can now be expressed as:

$$\begin{aligned} \chi(n, i; P_0) &= \chi_R(\tau_0) \\ &\quad\cdot\sum_{n=1}^{N}\exp(j\cdot\frac{4\pi\cdot\sin\theta_0\cdot x_n}{\lambda_c})\cdot\sum_{i=1}^{I}\exp(j\cdot\frac{4\pi\cdot\sin\phi_0\cdot y_i}{\lambda_c}) \\ &= \chi_R(\tau_0)\cdot\underbrace{\frac{\sin(\frac{2\pi}{\lambda_c}Nx_n\sin\theta_0)}{\sin(\frac{2\pi}{\lambda_c}x_n\sin\theta_0)}}_{\chi_A(P_0)}\cdot\underbrace{\frac{\sin(\frac{2\pi}{\lambda_c}Iy_i\sin\phi_0)}{\sin(\frac{2\pi}{\lambda_c}y_i\sin\phi_0)}}_{\chi_H(P_0)} \\ &= \chi_R(\tau_0)\cdot\chi_A(P_0)\cdot\chi_H(P_0) \end{aligned} \quad (7)$$

where $\chi_A(\Delta R_{n,i})$ is the azimuth fuzzy function, and $\chi_H(\Delta R_{n,i})$ is the height fuzzy function of the system. What can be concluded is the system's fuzzy function can be divided into three fuzzy functions along the range, azimuth and height directions under the far field. So, according to (4)and (7), the 3D resolutions respectively are:

$$\begin{aligned} \delta_r &= 0.886\cdot\frac{c}{2B} \\ \delta_a &= 0.886\cdot\frac{\rho\lambda_c}{2Nx_n} = 0.886\cdot\frac{\rho\lambda_c}{2L} \\ \delta_h &= 0.886\cdot\frac{\rho\lambda_c}{2Iy_i} = 0.886\cdot\frac{\rho\lambda_c}{2H} \end{aligned} \quad (8)$$

where B is the bandwidth of the transmitting signal; 0.886 is the width factor of the -3dB beam width; ρ is the target range; δ_r is the range resolution; δ_a and δ_h are the azimuth and height resolutions.

The main characteristics of the 3D GB-SAR system as shown in FIGURE 1 are summarized as follows:

1) Short aperture lengths in azimuth and height directions (1-4m): angle resolutions (-3dB beam width) are constant and space resolutions in cross-range directions (δ_a and δ_h) are increasing linearly with the increase of the range, as shown in (8).
2) Large antenna beam width in azimuth and height directions in order to illuminate the whole monitoring scene.
3) A large range scope: targets in near-field and far-field of the system are covered by the antenna illuminating.

The baseband range-compressed echo signal from the point P_0 is

$$\begin{aligned} &s_{rc}(t, x_n, y_i) \\ &= rect\left(\frac{x_n}{L}\right)rect\left(\frac{y_i}{H}\right) \\ &\quad\cdot p_r\left(t-\frac{2R\left(n, i; \vec{P}_0\right)}{c}\right)\exp\left[-j\frac{4\pi R\left(n, i; \vec{P}_0\right)}{\lambda_c}\right] \end{aligned} \quad (9)$$

where $p_r(t)$ is the compressed range envelope. The range history $R(n, i; P_0)$ is a key point affecting the range migration and azimuth and height modulation, which can be described as follows using the Taylor expansion at the aperture center ($x_n = 0, y_i = 0$):

$$\begin{aligned} &R(n, i; P_0) \\ &= \sqrt{x_n^2+y_i^2+\rho_0^2-2x_n\cdot\rho_0\sin\theta_0-2y_i\cdot\rho_0\sin\phi_0} \\ &\approx \rho_0-\sin\theta_0\cdot x_n-\sin\phi_0\cdot y_i+\frac{1-\sin\theta_0^2}{2\rho_0}\cdot x_n^2 \\ &\quad+\frac{1-\sin\phi_0^2}{2\rho_0}\cdot y_i^2-x_n\cdot y_i\cdot\frac{\sin\theta_0\sin\phi_0}{\rho_0} \\ &\quad+\frac{1}{6}\cdot\left[\begin{array}{l} y^3\cdot\left(3\cdot\frac{\sin\phi_0}{\rho_0^2}-3\cdot\frac{\sin^3\phi_0}{\rho_0^2}\right) \\ +3xy^2\left(\frac{\sin\theta_0}{\rho_0^2}-3\frac{\sin\theta_0\sin^2\phi_0}{\rho_0^2}\right) \\ +3x^2y\left(\frac{\sin\phi_0}{\rho_0^2}-3\frac{\sin^2\theta_0\sin\phi}{\rho_0^2}\right) \\ +x^3\cdot\left(3\cdot\frac{\sin\theta_0}{\rho_0^2}-3\cdot\frac{\sin^3\theta_0}{\rho_0^2}\right) \end{array}\right]+\widetilde{o}_{r4}(\cdot) \end{aligned} \quad (10)$$

Here, the higher order terms are contained in $\widetilde{o}_{r4}(\cdot)$ which is less significant given $L, H \ll \rho$. To further simplify the echo signal, we analyze the range history $R(n, i; P_0)$ of the range envelop term and the exponential order term in (9), to decide which term of $R(n, i; P_0)$ can be omitted under the system parameters in TABLE 1.

First, according to (10), the range cell migration ΔR in the range envelop term is,

$$\begin{aligned}
&\Delta R(n, i; P_0) \\
&= R(n, i; P_0) - \rho_0 \\
&= -\sin\theta_0 \cdot x_n - \sin\phi_0 \cdot y_i \\
&\quad + \frac{1-\sin^2\theta_0}{2\rho_0} \cdot x_n^2 + \frac{1-\sin^2\phi_0}{2\rho_0} \cdot y_i^2 - x_n \cdot y_i \cdot \frac{\sin\theta_0 \sin\phi_0}{\rho_0} + \tilde{o}_{r3}(\cdot) \\
&= \underbrace{-(\sin\theta_0 \cdot x_n + \sin\phi_0 \cdot y_i)}_{\Delta R_{linear}} \\
&\quad + \underbrace{\frac{1}{2\rho_0}\left[x_n^2 + y_i^2 - (\sin\theta_0 x_n + \sin\phi_0 y_i)^2\right]}_{\Delta R_{curvature}} + \tilde{o}_{r3}(\cdot)
\end{aligned} \tag{11}$$

where ΔR_{linear} is linear range migration, and $\Delta R_{curvature}$ is range curvature. If their absolute values are less than a quarter of the range resolution, they can be ignored. According to the system parameters, the maximum of ΔR_{linear} is,

$$|\Delta R_{linear}|_{\max} = |\sin\theta + \sin\phi|_{\max} \cdot L/2 \tag{12}$$

Under the system parameters in TABLE 1, it cannot always less than a quarter of the range resolution and should be considered.

The maximum of $\Delta R_{curvature}$ is,

$$|\Delta R_{curvature}|_{\max} = \frac{L^2}{4\rho_{\min}} \tag{13}$$

$\Delta R_{curvature}$ can be ignored when

$$|\Delta R_{curvature}|_{\max} = \frac{L^2}{4\rho_{\min}} < \frac{c}{8B_r} \tag{14}$$

That is

$$\rho_{\min} > \frac{2L^2 B_r}{c} \tag{15}$$

Next, the phase of echo signal in (9) is

$$\begin{aligned}
\psi_R\left(n, i; \vec{P}_0\right) &= -\frac{4\pi R\left(n, i; \vec{P}_0\right)}{\lambda_c} \\
&= -\frac{4\pi\rho_0}{\lambda_c} + \frac{4\pi}{\lambda_c} \cdot (\sin\theta_0 x_n + \sin\phi_0 y_i) \\
&\quad - \frac{2\pi}{\lambda_c \rho_0}\left[x_n^2 + y_i^2 - (\sin\theta_0 x_n + \sin\phi_0 y_i)^2\right] \\
&\quad + \frac{2\pi}{3\lambda_c} \cdot \left[\begin{array}{l}
y^3 \cdot \left(3 \cdot \frac{\sin\phi_0}{\rho_0^2} - 3 \cdot \frac{\sin^3\phi_0}{\rho_0^2}\right) \\
+3xy^2 \left(\frac{\sin\theta_0}{\rho_0^2} - 3\frac{\sin\theta_0 \sin^2\phi_0}{\rho_0^2}\right) \\
+3x^2 y \left(\frac{\sin\phi_0}{\rho_0^2} - 3\frac{\sin^2\theta_0 \sin\phi}{\rho_0^2}\right) \\
+x^3 \cdot \left(3 \cdot \frac{\sin\theta_0}{\rho_0^2} - 3 \cdot \frac{\sin^3\theta_0}{\rho_0^2}\right)
\end{array}\right] \\
&\quad + \widetilde{o}_{p4}(x_n; \rho_0, \theta_0)
\end{aligned} \tag{16}$$

When the absolute value of phase term is less than $\frac{\pi}{8}$, it can be ignored. The second-order term of the phase is $\psi_{quadratic}\left(n, i; \vec{P}_0\right)$

$$\begin{aligned}
&\left|\psi_{quadratic}\left(n, i; \vec{P}_0\right)\right| \\
&= \frac{2\pi}{\lambda_c \rho_0}\left[x_n^2 + y_i^2 - (\sin\theta_0 x_n + \sin\phi_0 y_i)^2\right] \le \frac{\pi L^2}{\lambda_c \rho_{\min}}
\end{aligned} \tag{17}$$

When we limit $\left|\psi_{quadratic}\left(n, i; \vec{P}_0\right)\right|_{\max} = \frac{\pi L^2}{\lambda_c \rho_{\min}} \le \frac{\pi}{8}$, we can get $\rho_{\min} \ge 8 \cdot \frac{L^2}{\lambda_c}$. It cannot be satisfied all the time in 3D GB-SAR system. So, the second-order $\psi_{quadratic}\left(n, i; \vec{P}_0\right)$ cannot be ignored.

$$\begin{aligned}
\chi(n, i; P_0) &= \sum_{n=1}^{N}\sum_{i=1}^{I}\int_{-\infty}^{\infty} s_t(t, x_n, y_i)\, s_r^*\left(t, x_n, y_i; P_0\right) dt \\
&= \sum_{n=1}^{N}\sum_{i=1}^{I} \cdot \int_{-\infty}^{\infty} \begin{array}{l} \text{rect}\left(\frac{t}{T_p}\right) \text{rect}\left(\frac{t-\tau_{n,i}}{T_p}\right) \exp\left(j2\pi f_c \tau_{n,i}\right) \\ \cdot \exp\left(j\pi K t^2\right) \exp\left(-j\pi K (t-\tau_{n,i})^2\right) dt \end{array} \\
&= \sum_{n=1}^{N}\sum_{i=1}^{I} \cdot \exp\left(j2\pi f_c \tau_{n,i}\right) \\
&\quad \underbrace{\cdot \int_{-\infty}^{\infty} \text{rect}\left(\frac{t}{T_p}\right) \text{rect}\left(\frac{t-\tau_{n,i}}{T_p}\right) \exp\left(j\pi K t^2\right) \exp\left(-j\pi K (t-\tau_{n,i})^2\right) dt}_{\chi_R(\tau_{n,i})}
\end{aligned} \tag{3}$$

The third-order term of the phase is $\psi_{cubic}\left(n,i;\vec{P}_0\right)$

$$\begin{aligned}&\left|\psi_{cubic}\left(n,i;\vec{P}_0\right)\right|\\&=\frac{2\pi}{3\lambda_c}\cdot\left[\begin{array}{l}y^3\cdot\left(3\cdot\frac{\sin\phi_0}{\rho_0^2}-3\cdot\frac{\sin^3\phi_0}{\rho_0^2}\right)\\+3xy^2\left(\frac{\sin\theta_0}{\rho_0^2}-3\frac{\sin\theta_0\sin^2\phi_0}{\rho_0^2}\right)\\+3x^2y\left(\frac{\sin\phi_0}{\rho_0^2}-3\frac{\sin^2\theta_0\sin\phi}{\rho_0^2}\right)\\+x^3\cdot\left(3\cdot\frac{\sin\theta_0}{\rho_0^2}-3\cdot\frac{\sin^3\theta_0}{\rho_0^2}\right)\end{array}\right]\\&\le\frac{\pi L^3}{2\lambda_c\rho_{\min}^2}\cdot|\sin\theta_0+\sin\phi_0|_{\max}\end{aligned}\tag{18}$$

we limit $\left|\psi_{cubic}\left(n,i;\vec{P}_0\right)\right|=\frac{\pi L^3}{2\lambda_c\rho_{\min}^2}\cdot|\sin\theta_0+\sin\phi_0|_{\max}\le\frac{\pi}{8}$, and get

$$\rho_{\min}\ge 2L\sqrt{\frac{L\cdot|\sin\theta+\sin\phi|_{\max}}{\lambda_c}}\tag{19}$$

Therefore, when the range ρ satisfies (15) and (19), we can retain $R(n,i;P_0)$ to the first-order of the range envelop term and the second-order of the exponential order term of the echo signal model in (9), ignoring the range curvature term in the range envelop term and high order terms in the phase. Consequently, it can be rewritten as:

$$\begin{aligned}&s_{rc}(t,x_n,y_i)\\&=rect\left(\frac{x_n}{L}\right)rect\left(\frac{y_j}{H}\right)\\&\cdot p_r\left(t-\frac{2\left(\rho_0-\sin\theta_0\cdot x_n-\sin\phi_0\cdot y_i\right)}{c}\right)\\&\cdot\exp\left\{\begin{array}{l}-j\frac{4\pi\rho_0}{\lambda_c}+j\frac{4\pi}{\lambda_c}\cdot\sin\theta_0\cdot x_n+j\frac{4\pi}{\lambda_c}\cdot\sin\phi_0\cdot y_i\\-j\frac{2\pi}{\lambda_c\rho_0}\left[x_n^2+y_i^2-(\sin\theta_0x_n+\sin\phi_0y_i)^2\right]\end{array}\right\}\end{aligned}\tag{20}$$

which is the base for following algorithm formulation. The simplified signal model demonstrates that the range migration of the echo signal is linear and the phase history is parabolic both in azimuth and height directions. Thus, the 3D-KSD algorithm is proposed. FIGURE 2 is the flowchart of the algorithm.

III. RANGE CELL MIGRATION CORRECTION

In order to focus the energy of the point P_0 on its range ρ_0, we apply Keystone formatting, which is a useful tool in SAR moving target processing [22], to realize RCMC. Firstly, (20)after Fourier transformation in range is

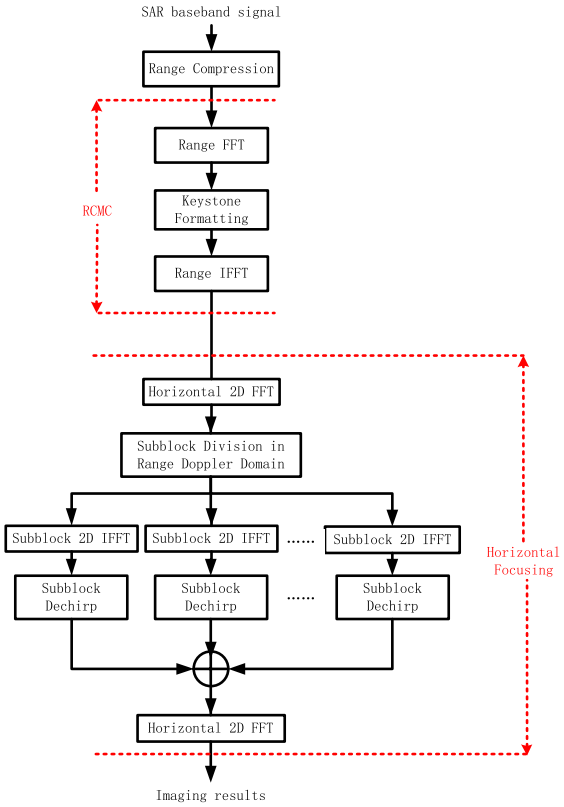

FIGURE 2. Processing flow of the 3D-KSD.

$$\begin{aligned}&S_{rc}(f,x_n,y_i)\\&=FFT\left\{s_{rc}(t,x_n,y_i)\right\}\\&=rect\left(\frac{x_n}{L}\right)rect\left(\frac{y_i}{H}\right)\cdot P_r(f)\\&\cdot\exp\left[\begin{array}{l}-j\frac{4\pi(f+f_c)\rho_0}{c}\\+j\frac{4\pi(f+f_c)}{c}\cdot\sin\theta_0\cdot x_n+j\frac{4\pi(f+f_c)}{c}\cdot\sin\phi_0\cdot y_i\end{array}\right]\\&\cdot\exp\left[-j\frac{2\pi}{\lambda_c\rho_0}\left[x_n^2+y_i^2-(\sin\theta_0x_n+\sin\phi_0y_i)^2\right]\right]\end{aligned}\tag{21}$$

where f is range baseband frequency; $P_r(\cdot)$ donates range envelope in frequency domain. Next, replace the azimuth variable x_n and the height variable y_i with $\frac{f_c}{f+f_c}x_m$ and $\frac{f_c}{f+f_c}y_j$ for each range frequency, so (21) can be rewritten as

$$\begin{aligned}&S_{rc-k}(f,x_m,y_j)\\&=S_{rc}(f,\frac{f_c}{f+f_c}x_m,\frac{f_c}{f+f_c}y_j)\\&=rect\left(\frac{x_m}{(f_c+f)/f_c\cdot L}\right)rect\left(\frac{y_j}{(f_c+f)/f_c\cdot H}\right)\cdot P_r(f)\\&\cdot\exp\left[\begin{array}{l}-j\frac{4\pi(f+f_c)\rho_0}{c}\\+j\frac{4\pi f_c}{c}\cdot\sin\theta_0\cdot x_m+j\frac{4\pi f_c}{c}\cdot\sin\phi_0\cdot y_j\end{array}\right]\\&\cdot\exp\left[-j\frac{2\pi}{\lambda_c\rho_0}\left[x_n^2+y_i^2-\left(\sin\theta_0x_m+\sin\phi_0y_j\right)^2\right]\right]\end{aligned}\tag{22}$$

where x_m and y_j are respectively the new azimuth variable and the new height variable after Keystone formatting. Lastly, the free of migration time signal after inverse-range Fourier transformation is described as

$$\begin{aligned} &s_{rc-k}(t, x_m, y_j) \\ &\approx rect\left(\frac{x_m}{L}\right) rect\left(\frac{y_j}{H}\right) p_r(t-\frac{2\rho_0}{c}) \\ &\cdot \exp\left[\begin{array}{l} -j\dfrac{4\pi\rho_0}{\lambda_c}+j\dfrac{4\pi}{\lambda_c}\cdot\sin\theta_0\cdot x_m+j\dfrac{4\pi}{\lambda_c}\cdot\sin\phi_0\cdot y_j \\ -j\dfrac{2\pi}{\lambda_c\rho_0}\left[x_m^2+y_j^2-\left(\sin\theta_0 x_m+\sin\phi_0 y_j\right)^2\right] \end{array}\right] \end{aligned} \tag{23}$$

Since $B_r/f_c \ll 1$ in 3D GB-SAR systems, we can simplify $rect\left(\frac{x_m}{(f_c+f)/f_c\cdot L}\right)$ in (23) to $rect\left(\frac{x_m}{L}\right)$, similarly, $rect\left(\frac{y_j}{(f_c+f)/f_c\cdot H}\right)$ to $rect\left(\frac{y_j}{H}\right)$. FIGURE 3 (left) shows the 3D range-compressed data distributed on a curved surface before RCMC and FIGURE 3 (right) shows the data laying on the flat surface after RCMC. The Keystone formatting focuses the energy of the point target in the range gate ρ_0.

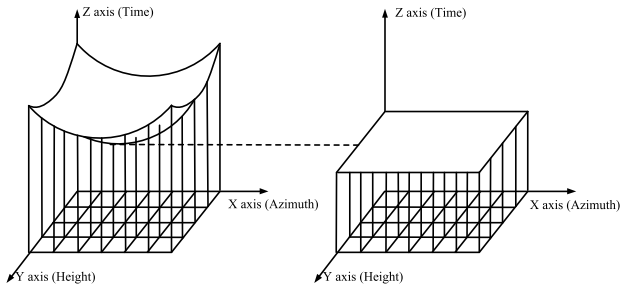

FIGURE 3. The point target's energy distribution before (left) and after Keystone formatting (right).

IV. AZIMUTH AND HEIGHT FOCUSING

The second part in FIGURE 2 aims to accomplish the azimuth and the height focusing. Firstly, equation (23) should be cross-range transformed into range-Doppler domain, that is, pseudo-spherical domain. In addition, the x_m's Fourier counterpart has a linear relation with $\sin\theta$ which is $f_m = 2\sin\theta/\lambda_c$ [22]; the y_j's Fourier counterpart has a linear relation with $\sin\phi$ which is $f_j = 2\sin\phi/\lambda_c$. Therefore, the transformed signal can be described in the $\rho-\sin\theta-\sin\phi$ domain. According to the principle of stationary phase, the relation between x_m and $\sin\theta$ can be written as

$$\begin{aligned} \sin\theta &= \sin\theta_0 - K_a\cdot x_m \\ x_m &= -\frac{1}{K_a}\left(\sin\theta-\sin\theta_0\right) \end{aligned} \tag{24}$$

Similarly, the relation between y_j and $\sin\phi$ is

$$\begin{aligned} \sin\phi &= \sin\phi_0 - K_p\cdot y_j \\ y_j &= -\frac{1}{K_p}\left(\sin\phi-\sin\phi_0\right) \end{aligned} \tag{25}$$

where K_a and K_p, the frequency modulation slopes of the azimuth and the height, are as following, respectively.

$$\begin{aligned} K_a(\rho_0,\theta_0) &= \frac{\cos^2\theta_0}{\rho_0} \\ K_p(\rho_0,\phi_0) &= \frac{\cos^2\phi_0}{\rho_0} \end{aligned} \tag{26}$$

Thus, the transformed signal in the $\rho-\sin\theta-\sin\phi$ domain is

$$\begin{aligned} &S(\rho,\sin\theta,\sin\phi;\rho_0,\theta_0,\phi_0) \\ &= FFT_{2D}\left\{s_{rc-k}(\frac{2\rho}{c},x_m,y_j)\right\} \\ &= rect\left(\frac{\sin\theta-\sin\theta_0}{L_{\sin\theta}(\rho_0,\theta_0)}\right)\cdot rect\left(\frac{\sin\phi-\sin\phi_0}{L_{\sin\varphi}(\rho_0,\varphi_0)}\right)\cdot p_r(\rho-\rho_0) \\ &\cdot\exp(-j\frac{4\pi\rho_0}{\lambda}+j\psi(\sin\theta,\sin\phi;\sin\theta_0,\sin\phi_0)) \end{aligned} \tag{27}$$

where $L_{\sin\theta}(\rho_0,\theta_0)$ is the width of support field in $\sin\theta$ domain, and $L_{\sin\phi}(\rho_0,\phi_0)$ is the width of support field in $\sin\phi$ domain

$$\begin{aligned} L_{\sin\theta}(\rho_0,\theta_0) &= K_a(\rho_0,\theta_0)\cdot L_a = \frac{L\left(1-\sin^2\theta_0\right)}{\rho_0} \\ L_{\sin\phi}(\rho_0,\varphi_0) &= K_p(\rho_0,\varphi_0)\cdot L_p = \frac{H\left(1-\sin^2\phi_0\right)}{\rho_0} \end{aligned} \tag{28}$$

We can observe the equation (23) which shows that different targets have the same azimuth support from $-L/2$ to $L/2$ and the same height support from $-H/2$ to $H/2$ in $\rho-x_m-y_j$ domain. Whereas, equation (27) shows that targets have segregated supports in the $\rho-\sin\theta-\sin\phi$ domain, centering on their angle coordinates $(\sin\theta_0,\sin\phi_0)$ with the azimuth extension $L_{\sin\theta}(\rho_0,\theta_0)$ and the height extension $L_{\sin\phi}(\rho_0,\varphi_0)$.

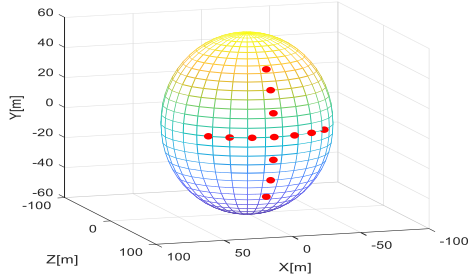

FIGURE 4. Diagram of the point targets position.

We illustrate the phenomenon in FIGURE 5. There are thirteen targets locating on the circle with a radius of 60 m. They are centering on (0,0), uniformly distributed with an interval of 15° along the azimuth and the height respectively shown in FIGURE 4. The signal after RCMC in $\rho-x_m\left(y_j\right)$ domain is shown in FIGURE 5 (a), in $\rho-\sin\theta$ $(\sin\phi)$ domain is shown in FIGURE 5 (b) and in $\sin\theta-\sin\phi$ domain is shown in FIGURE 5 (c). We can see that energy of different point targets after cross-range transformation is dramatically separated. Compared with the length of $\sin\theta$ and $\sin\phi$ axis, the targets' energy support is small. The blocking strategy as following is based on the energy-separation character of the 3D GB-SAR signal.

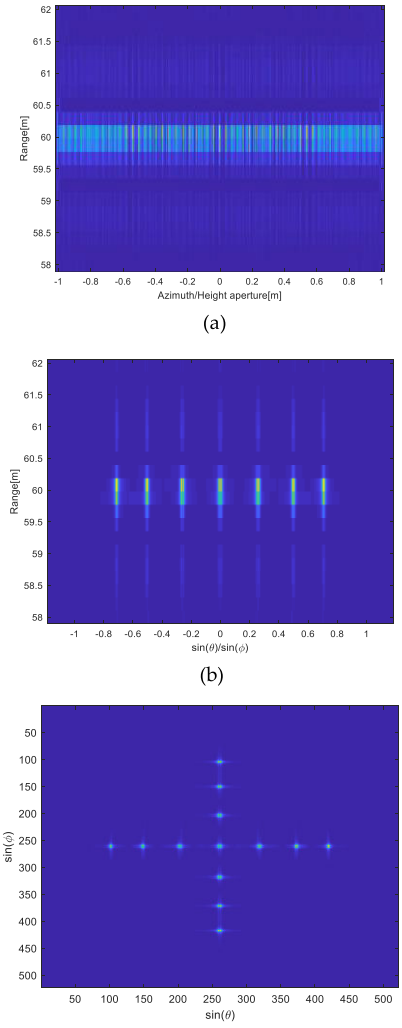

FIGURE 5. (a)ρ–$x_m\left(y_j\right)$ domain, (b)ρ–$\sin\theta\left(\sin\phi\right)$ domain and (c)$\sin\theta$–$\sin\phi$ domain.

A. AZIMUTH AND HEIGHT BLOCKING

Besides Keystone formatting, another key point in 3D-KSD algorithm is the cross-range (azimuth and height directions) blocking, by which targets in monitoring scene are segmented into several subblocks. The purpose of blocking is to realize azimuth and height focusing. Because of blocking, spatially variant dechirping can be applied to focus the targets with different K_a and K_p. The principle of blocking is given below at first and the derivation would be elaborated in detail later. Given a range gate ρ, the maximum width of blocks is

$$\Delta'(\rho) = \sqrt{|\sin\theta+\sin\phi|^2_{\max}+\frac{\rho\lambda}{4L^2}} - |\sin\theta+\sin\phi|_{\max}-\frac{L\left(2-\left(\sin^2\theta+\sin^2\phi\right)_{\max}\right)}{2\rho} \tag{29}$$

where $|\sin\theta+\sin\phi|_{\max}$ is the maximum absolute value of the sum of $\sin\theta$ and $\sin\phi$, and $\left(\sin^2\theta+\sin^2\phi\right)_{\max}$ is the maximum of the sum of $\sin^2\theta$ and $\sin^2\phi$. In order to simplify the blocking process, we limit the blocking width in azimuth direction is equal to that in height direction, that is, $\Delta'_{\sin\theta}(\rho) = \Delta'_{\sin\varphi}(\rho) = \Delta'(\rho)$. An example of 3D GB-SAR system parameters is given in TABLE 1, which is used for following derivation.

TABLE 1. Set of GB-SAR parameters.

Parameter	Symbol	Value
Carrier frequency	f_c	16.2 GHz
Bandwidth	B_r	600MHz
Aperture length in azimuth	L	2m
Aperture length in height	H	2m
Range	$\rho_{min}<\rho_o<\rho_{max}$	100-3000m
Azimuth angle	$\theta_{min}<\theta_o<\theta_{max}$	-45°~45°
Height angle	$\phi_{min}<\phi_o<\phi_{max}$	-45°~45°

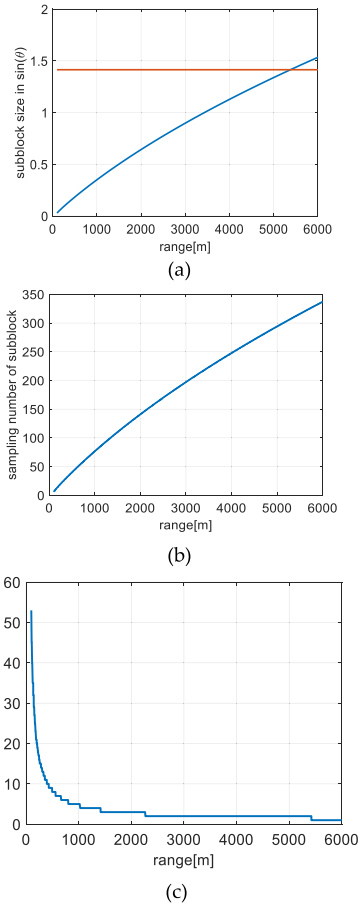

FIGURE 6. Azimuth blocking. (a) Blocking width $\Delta'_{\sin\theta}(\rho)$, (b) the number of sample points of the normal subblocks, and (c) the number of subblocks in each range.

Under the parameters in TABLE 1, FIGURE 6 (a) illustrates the variation of $\Delta'(\rho)$ with the variable ρ which shows that $\Delta'(\rho)$ increases as range ρ becomes larger. The minimum value of $\Delta'(\rho)$ is 0.0287 at the nearest range of 100m. When $\Delta'(\rho)$ is larger than the length of $\sin\theta$ or $\sin\phi$ axis, this dimension would not be divided into blocks. Considering effectiveness of computation, the width of blocks should be

equal to the upper limit of $\Delta'(\rho)$ in (29). Now, the blocking processing in azimuth direction is shown as following and illustrated in FIGURE 7.

1) At the range gate ρ, the number of sample points of each normal subblock is

$$n(\rho)=\begin{cases}\left\lfloor\dfrac{\Delta'(\rho)}{\upsilon_{\sin\theta}}\right\rfloor, & \left\lfloor\dfrac{\Delta'(\rho)}{\upsilon_{\sin\theta}}\right\rfloor\le N_a\\ N_a, & \left\lfloor\dfrac{\Delta'(\rho)}{\upsilon_{\sin\theta}}\right\rfloor> N_a\end{cases}\tag{30}$$

where $\upsilon_{\sin\theta}$ is the sampling interval in $\sin\theta$ axis, and the concept of the normal subblocks means blocks with the same number of points. N_a is the number of sample points of $\sin\theta$ axis, and $\lfloor\ \rfloor$ is to round down numbers.

2) The number of the subblocks in range gate ρ is,

$$m(\rho)=\left\lceil\frac{N_a}{n(\rho)}\right\rceil\tag{31}$$

where $\lceil\ \rceil$ is round up to numbers.

3) If N_a can be divided by $n(\rho)$ exactly, the N_a sample points of the range ρ can be uniformed segmented into $m(\rho)$ subblocks each with the number of points $n(\rho)$, as shown in the upper figure of FIGURE 7(a).

If N_a can be divided by $n(\rho)$ exactly with a remainder, the N_a sample points of the range ρ still will be segmented into $m(\rho)$ subblocks. The $m(\rho)-2$ subblocks have the same sample points $n(\rho)$, located in the middle of the $\sin\theta$ axis. The other two subblocks are located in the end of the $\sin\theta$ axis respectively with sample points $n_1(\rho)$ and $n_2(\rho)$, as shown in the lower figure of FIGURE 7 (a). $n_1(\rho)$ and $n_2(\rho)$ are two near integers and satisfy the next equation that is $n_1(\rho)+n_2(\rho)=n(\rho)+rem(N_a/n(\rho))$.

Following the instructions above are the same with the azimuth blocking processing in the reference [22] which presents the 2D-KSD algorithm. The results of azimuth blocking is shown in FIGURE 6 (b) and (c) according to the TABLE 1. In the simulation, the number of azimuth sample points is $N_a=512$, and the sample interval in $\sin\theta$ axis is $\upsilon_{\sin\theta}=0.0045$. Firstly, the length of the normal subblocks computed by (30) increases as the range gate ρ is bigger as illustrated in FIGURE 6(b). Then the number of subblocks $m(\rho)$ computed by (31) is shown in FIGURE 6(c). To ensure high accuracy, the nearer the range ρ is, the more the subblocks $m(\rho)$ are. At the nearest range of 100m, $m(\rho)$ is 53, and with the range ρ increasing, $m(\rho)$ decreases until it drops to 1 when the length of a subblock $n(\rho)$ is equal to the length of $\sin\theta$ axis. As a consequence, tighter blocking in near range and looser blocking in far range indicate the computational complexity descending, as shown in FIGURE 7(b). After $m(\rho)$ and $n(\rho)$ are obtained, step 3) and 4) give the procedures of the data segmentation of each range ρ. The height blocking instructions are the same with the azimuth and the number of subblocks is $p(\rho)$.

The blocking process can be achieved mathematically, that is, the (i,k) subblock can be obtained by the product of data and window function $W(\sin\theta,\sin\phi;\rho,i,k)$,i.e.,

$$\begin{aligned}&S_b(\sin\theta,\sin\phi;\rho,i,k)\\&=W(\sin\theta,\sin\phi;\rho,i,k)\cdot S(\rho,\sin\theta,\sin\phi;\rho_0,\theta_0,\phi_0)\\&=rect\left(\frac{\sin\theta-\sin\theta^i}{L^i_{\sin\theta}}\right)\cdot rect\left(\frac{\sin\phi-\sin\phi^k}{L^k_{\sin\phi}}\right)\\&\quad\cdot rect\left(\frac{\sin\theta-\sin\theta_0}{L_{\sin\theta}(\rho_0,\theta_0)}\right)\cdot rect\left(\frac{\sin\phi-\sin\phi_0}{L_{\sin\phi}(\rho_0,\varphi_0)}\right)\cdot p_r(\rho-\rho_0)\\&\quad\cdot\exp\left(-j\frac{4\pi\rho_0}{\lambda}+j\psi(\sin\theta,\sin\phi;\sin\theta_0,\sin\phi_0)\right)\\&=rect\left(\frac{\sin\theta-\sin\theta^i_0}{L^i_{\sin\theta_0}}\right)\cdot rect\left(\frac{\sin\phi-\sin\phi^k_0}{L^k_{\sin\phi_0}}\right)\cdot p_r(\rho-\rho_0)\\&\quad\cdot\exp\left(-j\frac{4\pi\rho_0}{\lambda}+j\psi(\sin\theta,\sin\phi;\sin\theta_0,\sin\phi_0)\right)\end{aligned}\tag{32}$$

where i and k mean the subblock is the ith in azimuth and the kth in height. The subscript '0' indicates the parameters about targets. The horizontal window function to obtain the horizontal subblock is

$$\begin{aligned}&W(\sin\theta,\sin\phi;\rho,i,k)\\&\quad=rect\left(\frac{\sin\theta-\sin\theta^i}{L^i_{\sin\theta}}\right)\cdot rect\left(\frac{\sin\phi-\sin\phi^k}{L^k_{\sin\phi}}\right)\end{aligned}\tag{33}$$

which means that the subblock's azimuth center, $\sin\theta^i$, azimuth length, $L^i_{\sin\theta}$, height center, $\sin\phi^k$ and height length, $L^k_{\sin\phi}$, all vary with the range ρ.

According to (32), the window function (33) segments the data support domain $rect\left(\frac{\sin\theta-\sin\theta_0}{L_{\sin\theta}(\rho_0,\theta_0)}\right)\cdot rect\left(\frac{\sin\phi-\sin\phi_0}{L_{\sin\phi}(\rho_0,\phi_0)}\right)$ into $rect\left(\frac{\sin\theta-\sin\theta^i_0}{L^i_{\sin\theta_0}}\right)rect\left(\frac{\sin\phi-\sin\phi^k_0}{L^k_{\sin\phi_0}}\right)$, as shown in FIGURE 7 (c). Reversely, connect all the segments and gain original data support profile.

$$\begin{aligned}&\sum_{i=1}^{m(\rho)}rect\left(\frac{\sin\theta-\sin\theta^i_0}{L^i_{\sin\theta_0}}\right)=rect\left(\frac{\sin\theta-\sin\theta_0}{L_{\sin\theta}(\rho_0,\theta_0)}\right)\\&\sum_{k=1}^{p(\rho)}rect\left(\frac{\sin\phi-\sin\phi^k}{L^k_{\sin\phi}}\right)=rect\left(\frac{\sin\phi-\sin\phi_0}{L_{\sin\phi}(\rho_0,\phi_0)}\right)\end{aligned}\tag{34}$$

B. SUBBLOCK DECHIRPING

Transform the $m(\rho)\cdot p(\rho)$ subblocks to x_m-y_j domain and get

$$\begin{aligned}&s_b(x_m,y_j;\rho,i,k)\\&=IFT_{\sin\theta}\left\{IFT_{\sin\phi}\left\{S_b(\sin\theta,\sin\phi;\rho,i,k)\right\}\right\}\\&=rect\left(\frac{x_m-x^i_0}{L^i_x}\right)\cdot rect\left(\frac{y_j-y^k_0}{L^k_y}\right)p_r(\rho-\rho_0)\\&\quad\cdot\exp\left[\begin{array}{l}-j\dfrac{4\pi\rho_0}{\lambda_c}+j\dfrac{4\pi}{\lambda_c}\cdot\sin\theta_0\cdot x_m+j\dfrac{4\pi}{\lambda_c}\cdot\sin\phi_0\cdot y_j\\-j\dfrac{2\pi}{\lambda_c\rho_0}\cdot\left[x_m^2+y_j^2-\left(\sin\theta_0x_m+\sin\phi_0y_j\right)^2\right]\end{array}\right]\end{aligned}\tag{35}$$

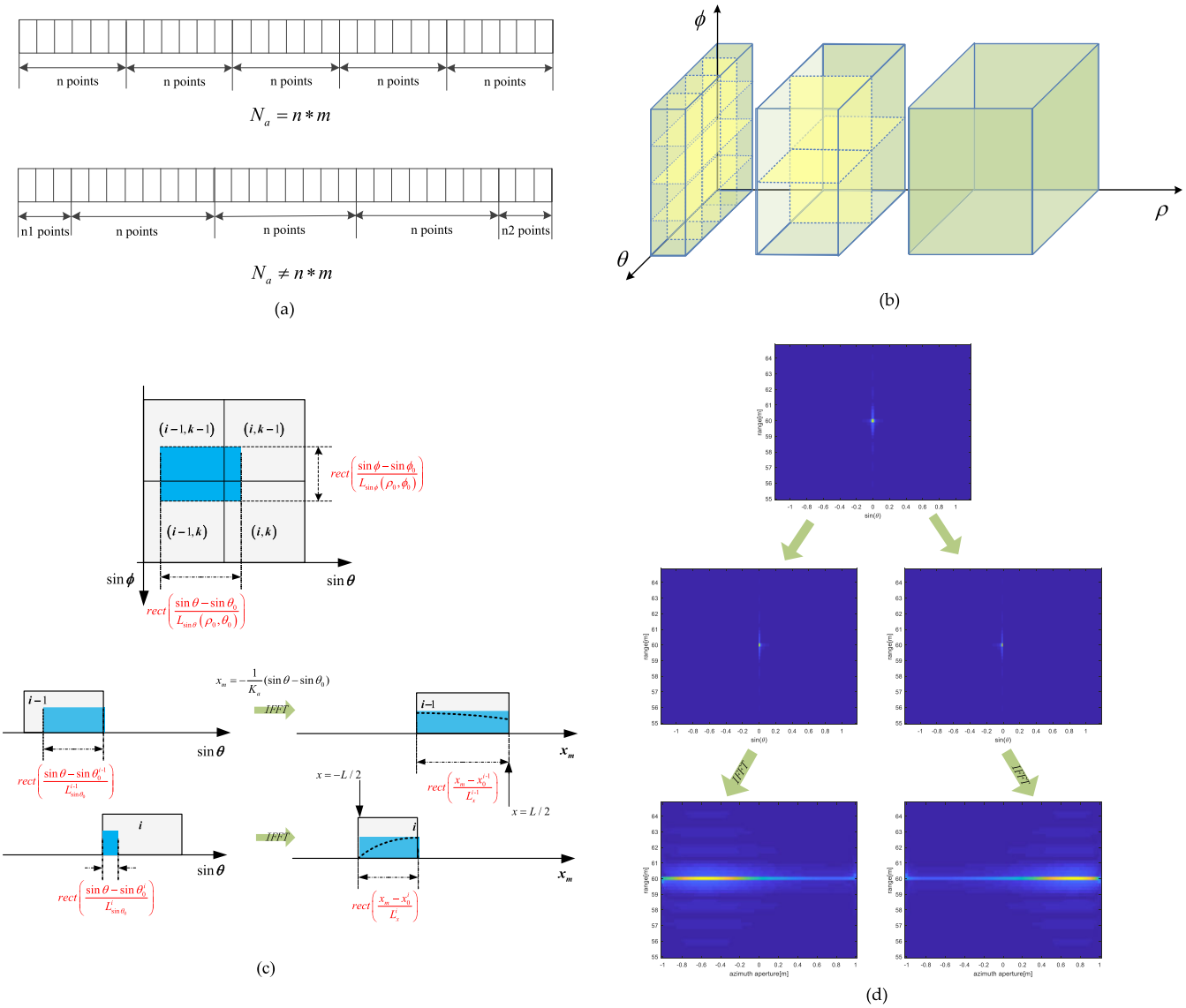

FIGURE 7. Horizontal blocking. (a) Blocking strategy, (b) segemation of the whole scene, (c) segmentation of a single target in $\sin\theta$ domain and x_m domian, and (d) simulations of the segmentation process.

where x_0^i presents the profile center of the (i,k) subblock and L_x^i is the profile length in x_m domain. y_0^k presents the profile center of the (i,k) subblock and L_y^k is the profile length in y_j domain. For the chirp signal, the division in $\sin\theta$ domain leads to the division in x_m domain. Using the linear relation in (24), the x_0^i and L_x^i can be described by $\sin\theta_0^i$ and $L_{\sin\theta_0}^i$

$$x_0^i = -\frac{1}{K_a}\left(\sin\theta_0^i - \sin\theta_0\right) \tag{36}$$

$$L_x^i = \frac{L_{\sin\theta_0}^i}{K_a\left(\rho_0,\theta_0\right)} \tag{37}$$

Connect all segments and obtain the original data profile, i.e.,

$$\sum_{i=1}^{m(\rho)} rect\left(\frac{x_m - x_0^i}{L_x^i}\right) = rect\left(\frac{x_m}{L}\right) \tag{38}$$

Similarly, the segmentation in $\sin\phi$ domain means the segmentation in y_j domain, and the y_0^k and L_y^k can be written as

$$y_0^k = -\frac{1}{K_p}\left(\sin\phi_0^k - \sin\phi_0\right) \tag{39}$$

$$L_y^k = \frac{L_{\sin\phi_0}^k}{K_p\left(\rho_0,\phi_0\right)} \tag{40}$$

All segments in y_j domain are connected to gain original data profile, i.e.,

$$\sum_{k=1}^{p(\rho)} rect\left(\frac{y_j - y_0^k}{L_y^k}\right) = rect\left(\frac{y_j}{H}\right) \tag{41}$$

FIGURE 7(c) and (d) illustrate the transformation process. The target data in $\sin\theta-\sin\phi$ domain are divided into four segments. We analyze the detail in $\rho-\sin\theta$ domain ($\sin\theta$

domain is the same with $\sin\phi$ domain). Then as shown in FIGURE 7 (c) and (d), data of the target P are segmented into two subblocks in $\sin\theta$ domain. Then the two subblocks are transformed into $\rho-x_m$ domain showing that the segmentation in $\sin\theta$ results in the segmentation in x_m domain.

Then all subblocks are dechirped by multiplying with reference signal in $\rho-x_m-y_j$ domain. The different reference signal is determined by the (i,k) subblock's center $(\sin\theta_i, \sin\phi_k)$ and the range ρ as below.

$$f_d\left(x_m, y_j; \rho; i, k\right) = \exp\left\{j\frac{2\pi}{\lambda_c\rho}\left[x_m^2+y_j^2-\left(\sin\theta^i x_m+\sin\phi^k y_j\right)^2\right]\right\} \tag{42}$$

Adding all the product of (35) and (42) at range gate ρ, the dechirped result is

$$\begin{aligned} &s_{de}\left(\rho, x_m, y_j; \rho_0, \theta_0, \phi_0\right) \\ &= \sum_{k=1}^{p(\rho)}\sum_{i=1}^{m(\rho)} s_b\left(x_m, y_j; \rho, i, k\right) f_d\left(x_m, y_j; \rho; i, k\right) \\ &= p_r\left(\rho-\rho_0\right) \\ &\quad \cdot \exp\left[-j\frac{4\pi\rho_0}{\lambda_c}+j\frac{4\pi}{\lambda_c}\sin\theta_0 x_m+j\frac{4\pi}{\lambda_c}\sin\phi_0 y_j\right] \\ &\quad \underbrace{\cdot \sum_{k=1}^{p(\rho)}\sum_{i=1}^{m(\rho)}\left\{\begin{array}{l} rect\left(\frac{x_m-x_0^i}{L_x^i}\right)\cdot rect\left(\frac{y_j-y_0^k}{L_y^k}\right) \\ \cdot \exp\left[j\frac{2\pi}{\lambda_c\rho}\left[\begin{array}{l}\left(\sin\theta^i x_m+\sin\phi^k y_j\right)^2 \\ -\left(\sin\theta_0 x_m+\sin\phi_0 y_j\right)^2\end{array}\right]\right]\end{array}\right\}}_{\varepsilon_{de}\left(\rho, x_m, y_j; \rho_0, \theta_0, \phi_0\right)} \end{aligned} \tag{43}$$

where the second line is what we want. The last line is residual phase error, denoted by $\varepsilon_{de}\left(\rho, x_m, y_j; \rho_0, \theta_0, \phi_0\right)$, introduced by the difference between the angle (θ^i, ϕ^k) of the reference signal and the angle (θ_0, ϕ_0) of the target.

Large value of $\varepsilon_{de}\left(\rho, x_m, y_j; \rho_0, \theta_0, \phi_0\right)$ would result in defocus or low phase accuracy. The denser the blocking is, which means $(\sin\theta^i, \sin\phi^k)$ is closer to the real value $(\sin\theta_0, \sin\phi_0)$, the smaller $\varepsilon_{de}\left(\rho, x_m, y_j; \rho_0, \theta_0, \phi_0\right)$ is. But denser blocking brings in large computation cost. Thus, in order to balance the imaging quality and the computational complexity, the 3D-KSD algorithm will take measures to control the phase error. Firstly, we limit the value of $\Delta'(\rho)$ mentioned above to ensure $\varepsilon_{de}\left(\rho, x_m, y_j; \rho_0, \theta_0, \phi_0\right) \le \pi/8$. Here, the phase error in range ρ_0 is

$$\begin{aligned} &\varepsilon_{de}\left(\rho, x_m, y_j; \rho_0, \theta_0, \phi_0\right) \\ &= \sum_{k=1}^{p(\rho)}\sum_{i=1}^{m(\rho)} rect\left(\frac{x_m-x_0^i}{L_x^i}\right)\cdot rect\left(\frac{y_j-y_0^k}{L_y^k}\right) \\ &\quad \cdot \exp\left[j\frac{2\pi}{\lambda_c\rho}\left[\left(\sin\theta^i x_m+\sin\phi^k y_j\right)^2\right.\right. \\ &\quad \left.\left.-\left(\sin\theta_0 x_m+\sin\phi_0 y_j\right)^2\right]\right] \end{aligned} \tag{44}$$

According to (38) and (41), each subblock has different and mutually exclusive data profiles, and the connection of the data profiles has consistent amplitude $rect\left(\frac{x_m}{L}\right) rect\left(\frac{y_j}{H}\right)$. So we only need to limit the phase $\left|\frac{2\pi}{\lambda_c\rho}\left[\left(\sin\theta^i x_m+\sin\phi^k y_j\right)^2-\left(\sin\theta_0 x_m+\sin\phi_0 y_j\right)^2\right]\right|$ to less than $\pi/8$ for any i and k.

$$\begin{aligned} &\left|\frac{2\pi}{\lambda_c\rho_0}\left[\left(\sin\theta^i x_m+\sin\phi^k y_j\right)^2-\left(\sin\theta_0 x_m+\sin\phi_0 y_j\right)^2\right]\right| \\ &\le \frac{\pi L^2}{2\lambda_c\rho_0} \\ &\quad \cdot\left(\left|\sin\theta_0+\sin\phi_0\right|\left(L_{\sin\theta}+L_{\sin\phi}+2\Delta\right)\right. \\ &\quad \left.+\frac{\left(L_{\sin\theta}+L_{\sin\phi}+2\Delta\right)^2}{4}\right) \end{aligned} \tag{45}$$

where $L_{\sin\theta}$ and $L_{\sin\phi}$ are the data support in the azimuth and height direction. The 3D GB-SAR system commonly has the same azimuth resolution and height resolution, so the lengths of the synthetic aperture in azimuth and height are the same $(L=H)$. Δ, the width of subblocks, needs to be determined $(\Delta_{\sin\theta}=\Delta_{\sin\phi}=\Delta)$. Under the limit of $\pi/8$, the maximum of Δ is

$$\begin{aligned} \Delta^{up}\left(\rho_0, \theta_0, \phi_0\right) &= \sqrt{\left|\sin\theta_0+\sin\phi_0\right|^2+\frac{\rho_0\lambda}{4L^2}} \\ &\quad -\left|\sin\theta_0+\sin\phi_0\right|-\frac{L\left(2-\sin^2\theta_0-\sin^2\phi_0\right)}{2\rho_0} \end{aligned} \tag{46}$$

According the parameters in TABLE 1, the blocking result Δ^{up} of the whole scene is shown in FIGURE 8.

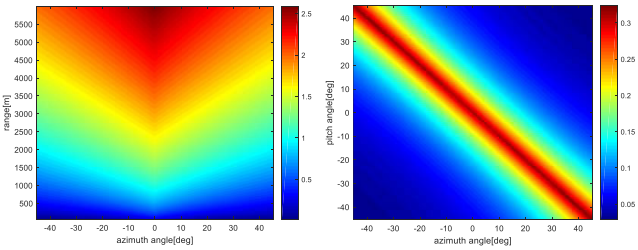

(a) (b)

FIGURE 8. The distribution of Δ^{up}. (a) In (ρ,θ) domain, when ϕ=0 and (b) in (θ,ϕ) domain when $\rho = 100m$.

It illustrates that Δ^{up} increases with the increase of range ρ_0 and the decrease of $|\sin\theta_0+\sin\phi_0|$. In addition, the variation of range has more influence than the angle on Δ^{up}. Here, in 3D-KSD, the minimum value Δ^{up} is chosen as the blocking width $\Delta'(\rho)$ in each range, i.e.,

$$\begin{aligned} \Delta'(\rho) &= \Delta^{up}\left(\rho, \left|\sin\theta+\sin\varphi\right|_{\max}\right) \\ &= \sqrt{\left|\sin\theta+\sin\varphi\right|_{\max}^2+\frac{\rho\lambda}{4L^2}} \\ &\quad -\left|\sin\theta+\sin\varphi\right|_{\max}-\frac{L\left(2-\left(\sin^2\theta+\sin^2\varphi\right)_{\max}\right)}{2\rho} \end{aligned} \tag{47}$$

$\Delta'(\rho)$ can satisfy the block width limit of all targets with different locations (θ_0, ϕ_0) in range ρ. It is exactly the blocking width given in (29). Under the limit of blocking width, the horizontal focus can be achieved by transforming (43) into $\sin\theta-\sin\phi$ domain.

$$\begin{aligned} &I_0(\rho, \sin\theta, \sin\phi; \rho_0, \theta_0, \phi_0) \\ &= FFT_{2D}\left\{s_{de}(\rho, x_m, y_j; \rho_0, \theta_0, \phi_0)\right\} \\ &= p_r(\rho-\rho_0)\cdot\mathrm{sinc}\left[\frac{2\pi L}{\lambda_c}(\sin\theta-\sin\theta_0)\right] \\ &\quad\cdot\mathrm{sinc}\left[\frac{2\pi H}{\lambda_c}(\sin\phi-\sin\phi_0)\right] \\ &\quad\cdot\exp\left(-j\frac{4\pi\rho_0}{\lambda_c}+j\Delta\phi(\rho_0, \theta_0, \phi_0)\right) \end{aligned} \tag{48}$$

where the profile is the ideal focus result. The limit of phase error $\pi/8$ is enough to meet the high phase precision requirement on most occasions.

C. APPLICABLE SCOPE AND COMPUTATIONAL COMPLEXITY

In this section, the comparison between 3D-KSD and other three 3D imaging algorithms (BPA and FPFA) is given below.

BPA has high imaging accuracy and can focus data both in the far-field and near-field, but high computational cost makes it not suitable for monitoring fast deforming targets. RMA also can obtain high-quality imaging results, but has strict requirements for the radar system's configuration as well as high computational cost. FPFA can only focus the far-field targets efficiently.

3D-KSD's applicable scope is determined by (15) and (19) i.e.,

$$\rho_{\min} > \max\left\{2\frac{L^2B_r}{c}, 2L\sqrt{\frac{L\cdot|\sin\theta+\sin\phi|_{\max}}{\lambda_c}}\right\} \tag{49}$$

where max {} indicates the maximum value of the input variable. We can see that the minimum range $\rho_{\min}$ and the angle scope $|\sin\theta+\sin\phi|_{\max}$ of the applicable scope are mutually restricted, as shown in FIGURE 9, and four sets of typical scene parameters are given in TABLE 2 according to (49). The larger the range is, the narrower the horizontal scene is.

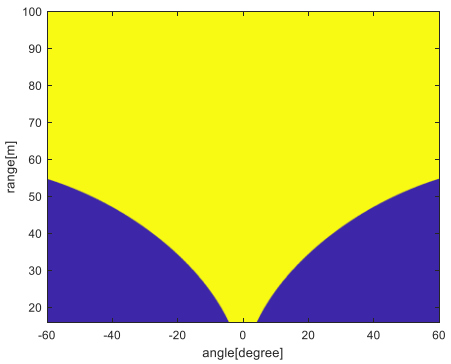

FIGURE 9. Applicable scope of 3D-KSD algorithm.

TABLE 2. Cases of applicable scope of 3D-KSD.

Number	Range scope R	Azimuth angular scope θ (same with height angular scope ϕ)
1	$R > 54.7m$	-60°~60°
2	$R > 49.5m$	-45°~45°
3	$R > 30m$	-15°~15°
4	$R > 17m$	-5°~5°

On the contrast, FPFA has a limited applicable scope given by

$$\rho > \frac{4L^2}{\lambda_c} \tag{50}$$

indicating the minimum range of imaging scope is 864m according to TABLE 1. So FPFA cannot obtain the near field imaging.

Then, the comparison on computational complexity of 3D-KSD and BPA is given using floating point operations (FLOPs) [18]. Assuming that the original dataset (after range compressed) is $N_r \times N_a \times N_p$, where N_r is the number of range sample points, N_a is the number of azimuth sample points, and N_p is the number of height sample points. Given that the interpolation kernel length is M_{ker}, and the number of subblocks in azimuth is $m(\rho)$, in height is $p(\rho)$. The calculation results of 3D-KSD's FLOPs is given in TABLE 3.

Assuming that in the dataset $N_a = N_p = N_r = N$, the computational complexity of 3D-KSD is $O\left(N^3\log(N)\right)$. However, the computational complexity of BPA is $O\left(N^4\right)$. Moreover, some existing methods based on FFT and complex multiplications are used to achieve Keystone formatting to reduce the computation further. It should be noted that, when the range increases, the number of subblocks decreases, resulting in the dramatically reduce of 3D-KSD's computation. In far field, the linear terms in $R(n, i; P_0)$ (10) is enough for focusing, so the 3D-KSD becomes to FPFA. At this time, the horizontal blocking is not needed, and the reference signal is 1. The focus in horizon can be achieved by FFT after RCMC, which makes 3D-KSD more efficient than BPA.

V. SIMULATIONS

To verify the feasibility of 3D-KSD and obtain its advantages compared with other 3D imaging algorithms, the imaging simulation experiments are given in this section. The system parameters are shown in TABLE 1.

First, the imaging process of the point target located in (60m, 30°, 30°) is given in FIGURE 10. FIGURE 10(a) gives the range-compressed signal before Keystone formatting, showing the obvious range cell migration in range-azimuth domain. FIGURE 10(b) shows that after Keystone formatting, the range cell migration is corrected and the target energy is totally centralized in the target range, 60 m. Then the data is transformed into $\rho-\sin\theta-\sin\phi$ domain. After data segmentation, the subblocks are obtained and inversely transformed into $\rho-x_m-y_i$ domain. By multiplying subblocks

TABLE 3. The computation cost of 3D-KSD.

Processing	Procedures	FLOPS
RCMC	Range FFT	$5N_r \log_2(N_r)\cdot N_a N_p$
	Keystone formatting	$4(2M_{\ker}-1)N_a N_p N_r$
	Range IFFT	$5N_r \log_2(N_r)\cdot N_a N_p$
	Subtotal	$10N_a N_p N_r \log_2(N_r)+4(2M_{\ker}-1)N_a N_p N_r$
Horizontal processing	Horizontal FFT	$5N_a N_p N_r \log_2(N_a N_p)$
	Dechirpping	$\left[5N_a N_p \log_2(N_a N_p)+8N_a N_p\right]\cdot\sum_{\rho=\rho(1)}^{\rho(N_r)} m(\rho)p(\rho)$
	Horizontal FFT	$5N_a N_p N_r \log_2(N_a N_p)$
	Subtotal	$10N_a N_p N_r \log_2(N_a N_p)+\left[5N_a N_p \log_2(N_a N_p)+8N_a N_p\right]\cdot\sum_{\rho=\rho(1)}^{\rho(N_r)} m(\rho)p(\rho)$
Total		$10N_a N_p N_r \log_2(N_a N_p N_r)+4(2M_{\ker}-1)N_a N_p N_r+\left[5N_a N_p \log_2(N_a N_p)+8N_a N_p\right]\cdot\sum_{\rho=\rho(1)}^{\rho(N_r)} m(\rho)p(\rho)$

with reference signals and summing subblocks in each range, the dechirping operation is finished. After the data being inversely Fourier transformed into $\rho-\sin\theta-\sin\phi$ domain, the horizontal focus is achieved as shown in FIGURE 10(c) and (d).

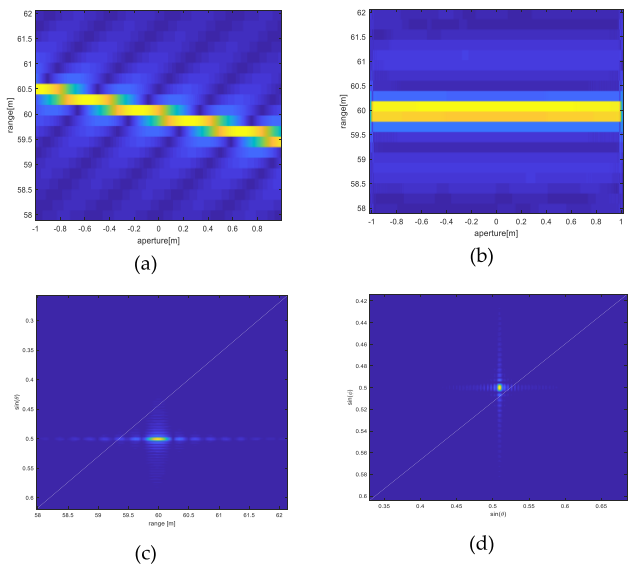

FIGURE 10. 3D-KSD imaging processing of a point target. (a) Signal after range compressed. (b) Signal after RCMC. (c) The imaging result in $(\rho, \sin\theta)$ domain. (d) The imaging result in $(\sin\theta, \sin\phi)$ domain.

The 3D imaging slice of the point target and one-dimensional imaging slice results along the range, azimuth and height are shown in FIGURE 11. We can see that the target is well focused and the performances of the three directions are dramatically good.

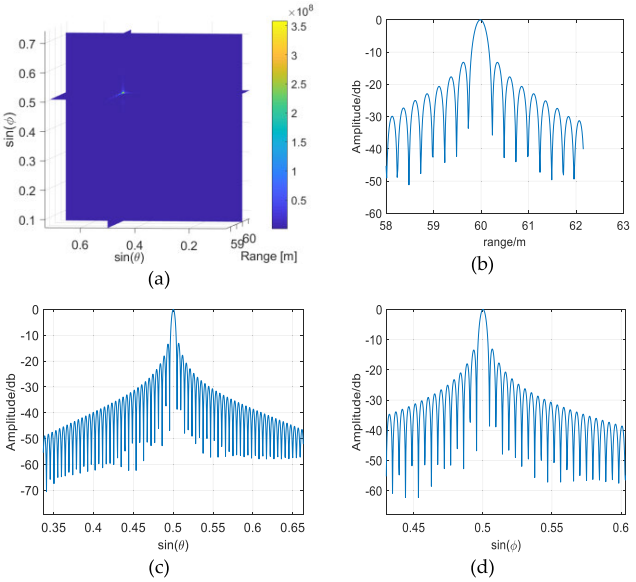

FIGURE 11. 3D imaging results of the point target at (60m, 30°, 30°). (a) The 3D slice map, (b) the slice map in range, (c) the slice map in azimuth, and (d) the slice map in height.

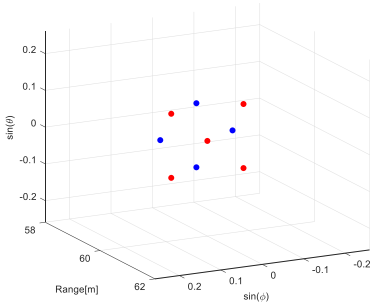

FIGURE 12. Nine distributed targets.

Second, to better validate 3D-KSD algorithm, a multi-target imaging experiment is carried out. FIGURE 12 shows locations of the nine distributed targets. The side view and front view of the distributed targets are given in FIGURE 13(a) and (c). FIGURE 13(b) and (d) demonstrate the imaging results.

We can see from FIGURE 13 (b), the side view and (d), the front view of the 3D imaging result that 3D-KSD has excellent focusing performance. In addition, the positions of focusing points in 3D imaging result are totally consistent with the targets position we set. This experiment validates that 3D-KSD is competent for multi-target imaging. Thus, 3D-KSD is qualified for imaging complex terrain.

Next, the comparison between 3D-KSD, BPA and FPFA is given by simulation data. First, there is a target at (60m, 0°, 0°), locating in the near-field of the radar aperture. FIGURE 14(a), (b), and (c) show the imaging results of the

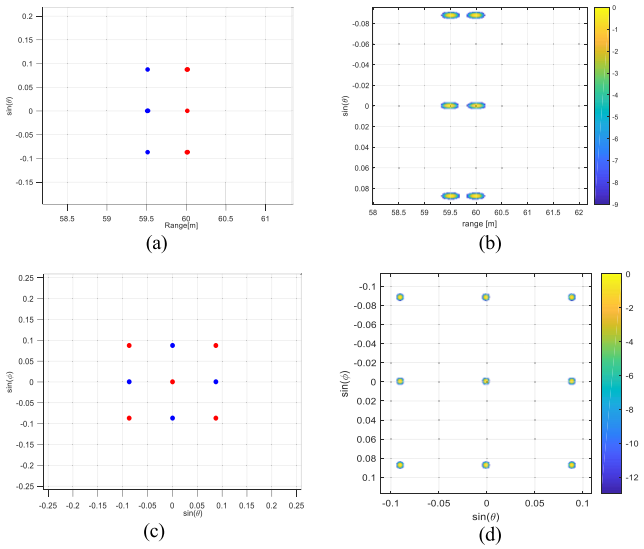

FIGURE 13. Imaging results of the targets in FIGURE 12.(a) Side view of targets. (b) Side view of 3D imaging result. (c) Front view of targets. (d) Front view of 3D imaging result.

TABLE 4. Performance of the three algorithms in far-field.

Performance	Theoretical value	3D-KSD	BPA	FPFA
$\sin\theta$ resolution (m)	2.05 (ρ=500m)	2.05	2.06	2.10
$\sin\phi$ Resolution (m)	2.05	2.06	2.07	2.09
Range resolution (m)	0.2215	0.2217	0.2218	0.2220
Range PSLR (dB)	-13.26	-13.15	-13.20	-13.24
Horizontal PSLR(dB)	-13.26	-13.08	-10.24	-10.38

TABLE 5. Computation time cost by algorithms.

Target position	3D-KSD	BPA	FPFA
(60m, 0°, 0°)	1.92s	38.5s	-
(500m, 0°, 0°)	1.98s	34.0s	0.82s

three algorithms. We can conclude that 3D-KSD has the same performance with BPA, and they are both valid in near-field. However, FPFA cannot focus the target. Then, FIGURE 14 (d), (e), and (f) show the imaging results of the target at (500m, 0°, 0°), in the far-field of the radar aperture. The target is well focused by the three algorithms. We can conclude that the three imaging algorithms have good performance in the case of far-field and the quantitative values are given in the TABLE 4.

In addition, the computation time required by imaging algorithms is given in TABLE 5. The time cost comparison of 3D-KSD, BPA and FPFA demonstrate the 3D-KSD has high computation efficiency in near-field and far-field while ensuring good focusing performance.

Finally, the performance comparison of 3D-KSD, BPA and FPFA is concluded. An imaging algorithm's performance includes focusing accuracy and computational complexity.

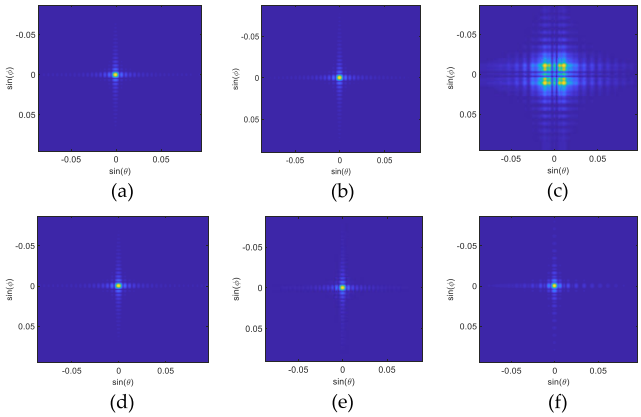

FIGURE 14. Imaging results of a point target at (60m, 0°, 0°) by (a) 3D-KSD, (b) BPA, (c) FPFA; and at (500m, 0°, 0°) by (d) 3D-KSD, (e) BPA, (f) FPFA.

TABLE 6. Comparison of 3D-KSD, BPA and FPFA.

Field	Performance	3D-KSD	BPA	FPFA
Near-field	Focusing accuracy	Good	Good	-
	Computational complexity	Medium	Poor	-
Far-field	Focusing accuracy	Good	Good	Good
	Computational complexity	Medium	Poor	Good

So VI gives the comparison result of imaging algorithms based on the two aspects in near-field and far-field. VI shows that, in far-field and near-field, 3D-KSD has lower computational complexity and the same high focusing accuracy with BPA. In far-field, FPFA is good in the two aspects. However, in near-field, FPFA cannot focus, so it cannot be used in the situation where both near-field and far-field imaging are required. In conclusion, the proposed method, 3D-KSD, is suitable for large range scope, high precision and real time imaging.

VI. CONCLUSION

This paper proposes a 3D imaging algorithm using for fast and accurate imaging of 3D GB-SAR system. It can be widely used for 3D GB-SAR imaging systems and most of 3D radar imaging systems with similar configurations and radar parameters. This method driven from the analysis and modeling of the echo data of 3D GB-SAR system is an algorithm based on Keystone formatting and Subblock Dechirping. In terms of RCMC, the Keystone formatting is used to eliminate the linear component of the echo data. Then the algorithm realizes the horizontal focus by subblock dechirping. The whole imaging process includes linear interpolation, FFTs and complex multiplications which dramatically save the computation cost. In addition, the 3D-KSD algorithm can be used in both near-field and far-field effectively. Thus, 3D-KSD can be used to monitor large range scope filed and obtain its 3D information. In addition, low computational complexity makes the proposed imaging algorithm fast enough to obtain the 3D tiny deformation of speedy

deforming targets such as landslides, buildings and structures and glacier snow mountains. The 3D GB-SAR system equipped with 3D-KSD is a powerful tool to predict geological disasters caused by tiny deformation.

REFERENCES

[1] D. Mecatti, G. Macaluso, A. Barucci, L. Noferini, M. Pieraccini, and C. Atzeni, "Monitoring open-pit quarries by interferometric radar for safety purposes," in *Proc. 7th Eur. Radar Conf.*, Oct. 2010, pp. 37–40.

[2] J. Severin, E. Eberhardt, L. Leoni, and S. Fortin, "Use of ground-based synthetic aperture radar to investigate the complex 3-D kinematics of a large pit slope," in *Proc. Slope Stability Int. Symp. Rock Slope Stability Open Pit Mining Civil Eng.*, 2011, pp. 18–21.

[3] G. Barla, F. Antolini, M. Barla, E. Mensi, and G. Piovano, "Monitoring of the beauregard landslide (Aosta valley, Italy) using advanced and conventional techniques," *Eng. Geol.*, vol. 116, nos. 3–4, pp. 218–235, Nov. 2010.

[4] W. H. Schulz, J. A. Coe, B. L. Shurtleff, J. Panosky, P. Farina, P. P. Ricci, and G. Barsacchi, "Kinematics of the Slumgullion landslide revealed by ground-based InSAR surveys," *Landslides Engineered Slopes, Protecting Soc. Through Improved Understand.*, vol. 2, pp. 1273–1279, Jun. 2012.

[5] D. Tapete, N. Casagli, G. Luzi, R. Fanti, G. Gigli, and D. Leva, "Integrating radar and laser-based remote sensing techniques for monitoring structural deformation of archaeological monuments," *J. Archaeological Sci.*, vol. 40, no. 1, pp. 176–189, Jan. 2013.

[6] H. Han and H. Lee, "Motion of Campbell glacier, east Antarctica, observed by satellite and ground-based interferometric synthetic aperture radar," in *Proc. 3rd Int. Asia–Pacific Conf. Synth. Aperture Radar (APSAR)*, Sep. 2011, pp. 1–4.

[7] D. Voytenko, T. H. Dixon, C. Werner, N. Gourmelen, I. M. Howat, P. C. Tinder, and A. Hooper, "Monitoring a glacier in southeastern iceland with the portable terrestrial radar interferometer," in *Proc. IEEE Int. Geosci. Remote Sens. Symp.*, Jul. 2012, pp. 3230–3232.

[8] H. S. Stone, M. T. Orchard, E.-C. Chang, and S. A. Martucci, "A fast direct Fourier-based algorithm for subpixel registration of images," *IEEE Trans. Geosci. Remote Sens.*, vol. 39, no. 10, pp. 2235–2243, Oct. 2001.

[9] L. Ferro-Famil, S. Tebaldini, M. Davy, C. Leconte, and F. Boutet, "Very high-resolution three-dimensional imaging of natural environments using a tomographic ground-based SAR system," in *Proc. 8th Eur. Conf. Antennas Propag. (EuCAP)*, Apr. 2014, pp. 3221–3224.

[10] J. Stephen, "Design and feasibility testing for a ground-based, threedimensional, ultra-high-resolution, synthetic aperture radar to image snowpacks," M.S. thesis, Brigham Young Univ., Provo, UT, USA, Aug. 2010.

[11] Z. Ding, Y. Li, W. Liu, Y. Xiang, Y. Zhao, H. Liu, T. Zeng, and T. Long, "Near-field phase cross correlation focusing imaging and parameter estimation for penetrating radar," *IEEE Trans. Geosci. Remote Sens.*, vol. 58, no. 1, pp. 598–611, Jan. 2020.

[12] A. D. X. Chen Wang Ma, "An improved BP algorithm for high-resolution MIMO imaging radar," in *Proc. Int. Conf. Audio, Lang. Image Process.*, Nov. 2010, pp. 1663–1667.

[13] S. S. Ahmed, A. Schiess, and L.-P. Schmidt, "Near field mm-wave imaging with multistatic sparse 2D-arrays," in *Proc. Eur. Radar Conf. (EuRAD)*, Oct. 2009, pp. 180–183.

[14] J. Fortuny-Guasch, "A fast and accurate far-field pseudopolar format radar imaging algorithm," *IEEE Trans. Geosci. Remote Sens.*, vol. 47, no. 4, pp. 1187–1196, Apr. 2009.

[15] G. C. Ian and H. W. Frank, *Digital Processing of Synthetic Aperture Radar Data: Algorithm and Implementation*. Boston, MA, USA: Artech House, 2005, pp. 113–128.

[16] C. Caffario, C. Prati, and F. Rocca, "SAR data focusing using seismic migration techniques," *IEEE Trans. Aerosp. Electron. Syst.*, vol. 27, no. 2, pp. 194–207, Mar. 1991.

[17] Y. Li, X. Wang, and Z. Ding, "Multi-target position and velocity estimation using OFDM communication signals," *IEEE Trans. Commun.*, vol. 68, no. 2, pp. 1160–1174, Feb. 2020.

[18] I. G. Cumming and F. H. Wong, *Digital Processing of Synthetic Aperture Radar Data: Algorithm and Implementation*. Boston, MA, USA: Artech House, 1995, pp. 120–134.

[19] D. R. Wehner, *High Resolution Radar*. Norwood, MA, USA: Artech House, 1987, pp. 38–45.

[20] W. Tian, Z. Zhao, C. Hu, J. Wang, and T. Zeng, "GB-InSAR-Based DEM generation method and precision analysis," *Remote Sens.*, vol. 11, no. 9, p. 997, 2019.

[21] C. Hu, J. Wang, W. Tian, R. Wang, H. Li, and L. Zhu, "Generalized ambiguity function properties of ground-based wideband MIMO imaging radar," *IEEE Trans. Aerosp. Electron. Syst.*, vol. 55, no. 2, pp. 578–591, Apr. 2019.

[22] R. P. Perry, R. C. DiPietro, and R. L. Fante, "SAR imaging of moving targets," *IEEE Trans. Electron. Syst.*, vol. 35, no. 1, pp. 188–200, Jan. 1999.

[23] T. Zeng, C. Mao, C. Hu, and W. Tian, "Ground-based SAR wide view angle full-field imaging algorithm based on keystone formatting," *IEEE J. Sel. Topics Appl. Earth Observ. Remote Sens.*, vol. 9, no. 6, pp. 2160–2170, Jun. 2016.

WEIMING TIAN was born in 1983. He received the B.S. and Ph.D. degrees from the Beijing Institute of Technology, Beijing, China, in 2005 and 2010, respectively. He is currently working with the School of Information and Electronics, Beijing Institute of Technology. His research interests include SAR system and signal processing, bistatic SAR synchronization, high-resolution radar systems, real-time radar signal processing, and DInSAR technology.

WENYU YANG received the B.S. degree in information and electronic engineering from the Beijing Institute of Technology, Beijing, China, in 2017, where she is currently pursuing the master's degree with the School of Information and Electronics. She is major in ground-based synthetic aperture radar signal processing and three-dimensional multiple-input and multiple-output signal processing.

TONGXIN DANG was born in Shijiazhuang, China, in 1977. He received the B.S. and M.S. degrees from the Zhengzhou Information Science and Technology Institute, in 2000 and 2005, respectively. He is currently pursuing the Ph.D. degree in radar signal processing with the PLA Strategic Support Force Information Engineering University. His research interests are SAR and ISAR imaging.

ZHENG ZHAO was born in Beijing, China, in 1994. He received the B.S. degree from the Beijing Institute of Technology, Beijing, in 2016, where he is currently pursuing the Ph.D. degree in interferometric SAR system and data processing. His research interests include SAR data processing, SAR interferometry technique, and GB-InSAR system design.

XIAOXIN HAN received the B.S. degree from the Beijing Institute of Technology, Beijing, China, in 2017, where she is currently pursuing the M.S. degree with the School of Information and Electronics. She was major in synthetic wideband radar signal processing.